Biosensors and Bioelectronics 133 (2019) 72–78

Contents lists available at ScienceDirect

Biosensors and Bioelectronics

journal homepage: www.elsevier.com/locate/bios

Thionin functionalized signal amplification label derived dual-mode electrochemical immunoassay for sensitive detection of cardiac troponin I

Hui Lv, Yueyun Li*, Xiaobo Zhang, Xinjin Li, Zhen Xu, Lei Chen, Degang Li*, Yunhui Dong

School of Chemistry and Chemical Engineering, Shandong University of Technology, Zibo 255049, PR China

ARTICLE INFO

Keywords:
Sandwich-type electrochemical immunosensor
Double signal label
Cardiac troponin I
Differential pulse voltammetry
Amperometric i-t

ABSTRACT

A sensitive sandwich-type electrochemical immunosensor was established by employing Au@Pt core-shell multi-branched nanoparticles, and thionin functionalized nitrogen/sulfur co-doped graphene oxide (N/S-cGO/L-lys/Au@Pt MBs/Thi) as a double signal label to detect cardiac troponin I (cTnI). In this work, Au nanorods functionalized polydopamine (Au NR@PDA) with high adsorption capacity and superior electroconductivity can provide an efficient substrate for immobilizing primary antibodies (Ab_1). In the proposed N/S-cGO/L-lys/Au@Pt MBs/Thi, an electrochemically active molecule, Thi was covalently bonded in the N/S-cGO/L-lys/Au@Pt MBs. It presented a strong differential pulse voltammetry (DPV) current signal without electron transfer mediators, and showed a high electrocatalytic activity toward H_2O_2 reduction by using amperometric i-t (*i-t*). Impressively, with the synergistic effect of N/S-cGO/L-lys/Au@Pt MBs/Thi and Au NR@PDA, the developed dual-mode electrochemical immunosensor for cTnI detection showed a wide linear concentration range (50 fg/mL to 250 ng/mL, 750 fg/mL to 100 ng/mL) and a low detection limit (16.7 fg/mL, 250 fg/mL) via *i-t* and DPV, respectively. Furthermore, this immunosensor exhibited acceptable reproducibility, high sensitivity and good stability under optimal conditions. More importantly, the satisfactory results were obtained in detection of cTnI-spiked human serum samples, and the presented method may be a promising application in clinical bioanalysis.

1. Introduction

Electrochemical methodology as a useful tool, owing to its intrinsic advantages of remarkable selectivity, ease of operating and fast response, has been widely used in areas, like food safety control, environmental monitoring and medical analysis (Asif et al., 2018; Wen et al., 2016; Liu et al., 2017). As a branch of electrochemical methodology, a sandwich-type electrochemical immunoassay is promising to apply in early clinical diagnosis and analysis of disease states (Lv et al.al., 2018b; Zhang et al., 2019, 2018d). To construct a highly efficient sandwich-type electrochemical immunosensor, three strategies would generally be utilized: (1) Improving conductivity of electrode modification material to accelerate electron transfer (Li et al., 2018; Yáñez-Sedeño et al., 2016); (2) Increasing the loading number of antibodies by using some materials as carriers to ensure the possibility of immunoreaction (Yang et al., 2018; Zhang et al., 2018b); (3) Amplifying the detectable signal with multi-functional label to effectively improve the performance of immunosensor (Zhang et al., 2018a).

The primary antibodies (Ab_1) immobilization plays a crucial role in sandwich-type immunoassay, and one of the most common methods is to employ substrate material with the carboxylic acid or amine groups as a bridge to immobilize Ab_1 (Shen et al., 2018). Dopamine (DA) with special structure can polymerize to form PDA film at pH = 8.5 and contain a large number of hydrophilic groups (Zhou and Liu, 2017). Therefore, the as-fabricated PDA film can serve as a cross-linker reagent, which not only captures and immobilizes Ab_1 effectively by Michael reactions but can adhere to electrode surface to improve the stability of materials (Zhang et al. 2018c; Zhou et al., 2014). However, the application of PDA was limited for its relatively low conductivity properties. To address this challenge, Au nanorods (Au NR) were selected as an ideal nanoparticle to functionalize PDA, which featured superior electron transfer ability and good biocompatibility (Zhang et al., 2014a, 2014b). Consequently, the formed Au nanorods functionalized polydopamine (Au NR@PDA) can enhance conductivity and be used as an electrode modified material in fabrication of sandwich-type immunosensor.

Recently, noble metal nanoparticles (NPs) have attracted widespread attention due to their preferable electronic conductivity, catalytic property and good biocompatibility (Cho et al., 2018; Lai et al., 2019). Among various NPs, Au@Pt core-shell multi-branched nanoparticles (Au@Pt MBs) exhibited better peroxidase-like property than other species, because of the electronic effect and synergistic effect

* Corresponding authors.
E-mail addresses: liyueyun@sdut.edu.cn (Y. Li), ldg@sdut.edu.cn (D. Li).

https://doi.org/10.1016/j.bios.2019.03.033
Received 25 January 2019; Received in revised form 17 March 2019; Accepted 18 March 2019
Available online 18 March 2019
0956-5663/

between Au and Pt (He et al., 2018; Lai et al., 2018). In addition, abundant binding sites expressed on the surface of the multi-branched structure could further enhance the catalytic activity for H_2O_2 reduction (Lv et al., 2018a). Except for catalytic property, Au@Pt MBs with better biocompatibility could increase the number of antibodies through interaction between the amine group of antibodies and noble metal NPs (Gao et al., 2018). In order to reduce the costs and retain the catalytic efficiency of noble metal NPs, Au@Pt MBs were decorated onto the surface of nitrogen/sulfur co-doped graphene oxide (N/S-cGO) by using L-lysine with NH_2 and COOH as a bridge and linker, and this lead to the formation of N/S-cGO/L-lys/Au@Pt MBs nanomaterials (Zhang et al., 2010). Compared with bare GO, N/S-cGO presented unique property due to strong synergetic effects between heteroatom dopants (Hu et al., 2016), and it displayed enhanced sensing properties with higher specific surface area and better stability (Shen et al., 2015). Furthermore, as an important functional material of electron mediators, thionin (Thi) could mediate electrocatalytic reduction H_2O_2 and further improve the catalytic ability of the amplifier (Zhai et al., 2016). Meanwhile, it can be directly used as a redox probe for an electrochemical signal. As a result, N/S-cGO/L-lys/Au@Pt MBs were served as nanocarriers to anchor Thi to obtain a double signal label (N/S-cGO/L-lys/Au@Pt MBs/Thi).

Acute myocardial infarction (AMI) is one of the most prevalent causes for human death both in developing and developed countries (Spain et al., 2018). Cardiac troponin I (cTnI, molecular weight, 24 kDa) has excellent cardiac specificity and is always acknowledged as a principal biomarker for AMI, which can provide a long detecting window for cardiac injury (Ye et al., 2018). In this work, cTnI was used as a model analyze and a high-efficient dual-mode electrochemical strategy was designed. Utilizing Au NR@PDA as an electrode substrate material can increase loading amount of Ab_1, N/S-cGO/L-lys/Au@Pt MBs/Thi not only as signal amplifier for detecting cTnI via amperometric *i-t* toward the reduction of H_2O_2, but also can be directly used as redox probe for electrochemical signal readout via differential pulse voltammetry (DPV) achieved in buffer solution at low positive potential. Importantly, the developed immunosensor exhibited improved analytical performance, implying the immunosensor had bright application in the early diagnosis of various diseases.

2. Experimental

2.1. Preparation of the cTnI immunosensor

Fig. 1A showed the preparation procedure of N/S-cGO/L-lys/Au@Pt MBs/Thi-Ab_2 (Ab_2 label). First, 1.0 mL of Ab_2 solution (20.0 μg/mL) was added into 1.0 mL of N/S-cGO/L-lys/Au@Pt MBs/Thi (6.0 mg/mL) and oscillated for 8 h at 4 °C to obtain Ab_2 coated N/S-cGO/L-lys/Au@Pt MBs/Thi with formation. Then the obtained Ab_2 label was collected by centrifugation and re-dispersed in PBS (2.0 mL, pH = 7.0), and finally stored at 4 °C before use.

Fig. 1B illustrated the sandwich-type electrochemical immunosensor fabrication process. Before the modification, alumina slurries (300 and 50 nm) were used to polish the bare GCE, followed by washing with ultrapure water to obtain a mirror-like surface. Subsequently, 7.0 μL of the as-prepared Au NR@PDA solution was first modified the cleaned GCE and dried at room temperature. Next, 6.0 μL of Ab_1 (10.0 μg/mL) was incubated on the formed film via Au-NH_2 bonds at 4 °C, followed by resulting electrode was washed with the PBS to remove the physically absorbed Ab_1. Then 3.0 μL of BSA (1 wt%) was coated on the surface of the modified electrode to eliminate the non-

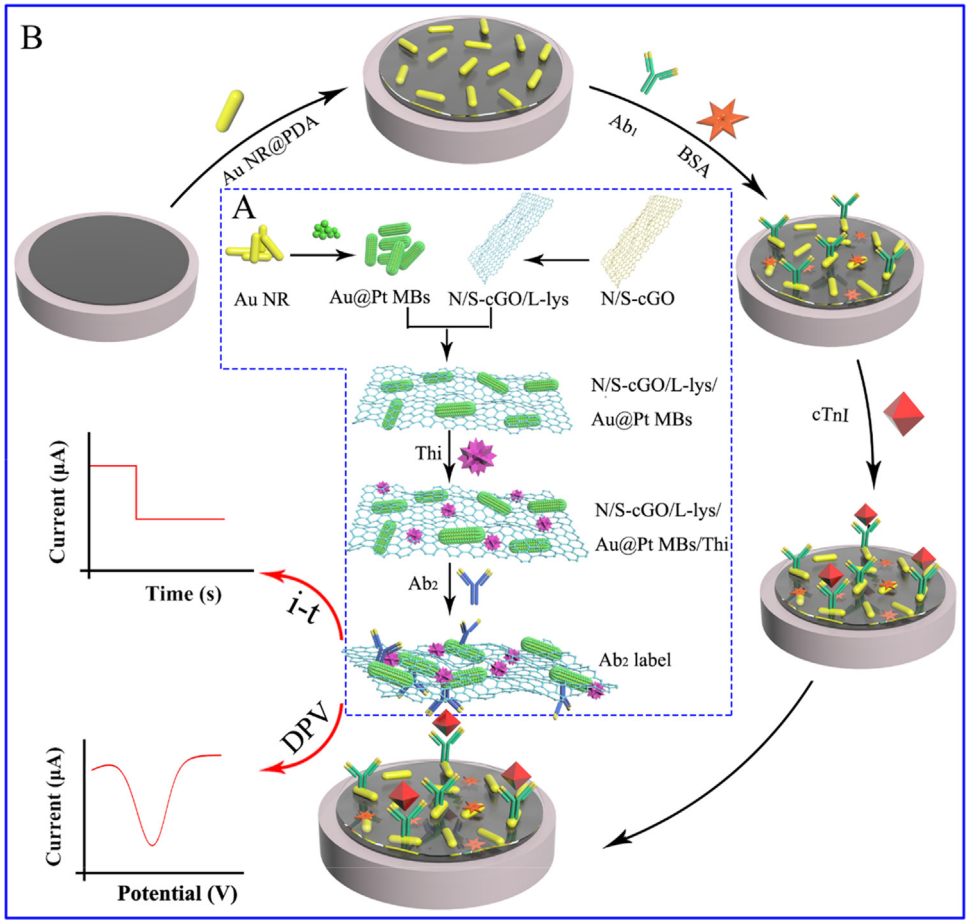

Fig. 1. (A) Preparation process of Ab_2 label. (B) The fabrication process of the sandwich-type cTnI immunosensor.

specific active sites. And then, the redundant BSA was removed by washing with PBS and dried naturally. Based on the sandwich format, the modified GCE was incubated with varying concentrations of cTnI. Finally, 6.0 μL of Ab_2 label (3.0 mg/mL) was added to the surface of electrode to form the immunocomplex. The sandwich-type electrochemical immunosensor was fabricated completely and stored at a refrigerator (4 °C) for further research. The details preparation process of Au NR@PDA and N/S-cGO/L-lys/Au@Pt MBs/Thi are provided in Supplementary material (SM).

2.2. Measurements of the fabricated immunosensor

The fabricated immunosensor tested through *i-t* was scanned at the potential of −0.4 V. After the signal background remained stable, 10 μL of H_2O_2 (5.0 mol/L) was injected into the PBS solution under mild stirring. Subsequently, DPV was scanned from −0.4 to 0 V directly in 10 mL of PBS (pulse amplitude: 50 mV, and pulse period: 500 ms). Electrochemical impedance spectroscopy (EIS) was recorded in a solution including 2.5 mM $[Fe(CN)_6]^{3-/4-}$ and 0.1 M KCl (frequency range: 10^{-1} to 10^5 Hz, and initial voltage: 0.24 V). All the materials and apparatus are provided in SM.

3. Results and discussion

3.1. Characterization of Au NR@PDA

Morphology and size of the as-prepared Au NR were characterized by SEM and TEM. SEM image (Fig. 2A) clearly showed almost all the particles were rod in shape. Fig. 2B displayed the corresponding TEM image of Au NR, indicating the obtained Au NR were nearly monodispersed with an average length of 100 nm and an average diameter of 20 nm. The morphologies of the produced nanomaterials were characterized by SEM. Compared with Au NR, the Au NR@PDA (Fig. 2C) showed a rougher surface, indicating that the Au NR have been enwrapped by PDA film. Meanwhile, EDS spectrum (Fig. S1) displayed distinct signal of C, N, O and Au, confirming the elemental composition of the Au NR@PDA. For investigate whether the Au NR@PDA composite can meet the needs of a cyclic potential scan for the long testing process, the stability of Au NR@PDA was tested by CV in 5.0 mM $K_3[Fe(CN)_6]$ containing 0.1 M KCl. As seen in Fig. 2D, there was no obvious change of the redox peak current and peak potential after Au NR@PDA modified bare glassy carbon electrode (GCE) in the same sweep speed (50 mV/s) continuous sweep 60 times, which explained the Au NR@PDA had good electrochemical stability.

The electrode effective surface area for Au NR@PDA was obtained by chronocoulometry (Fig. 2E) based on Anson equation (Anson, 1964).

$$Q(t) = \frac{2nFACD^{1/2}t^{1/2}}{\pi^{1/2}} + Q_{dl} + Q_{ads}$$

where C is substrate concentration, D is the diffusion coefficient, n is electron transfer number, Q_{dl} is double layer charge which could be eliminated by background subtraction, Q_{ads} is Faradic charge. By calculating the slopes of the plot of Q-$t^{1/2}$ curves (Fig. 2F), we obtained the electroactive surface areas (A) of different electrodes: GCE (0.092 cm^2), Au NR/GCE (0.123 cm^2) and Au NR@PDA/GCE (0.139 cm^2), indicating the electrochemical effective surface area increased obviously after the modification process.

The electrochemical properties for Au NR@PDA were performed by CV at different scan rates. As shown in Fig. 2G, with a scant rate ranging from 10 mV/s to 300 mV/s, both of the anodic peak current (I_{pa}) and the cathodic peak current (I_{pc}) increased as well. The two linear regression equations are as follows (Fig. 2H): I_{pa} (μA) = 12.4808 + 10.4683 $v^{1/2}$ (mV/s) (R = 0.99772) and I_{pc} (μA) = −13.4685 − 9.201 $v^{1/2}$ (mV/s) (R = 0.99402). This behavior is characteristic of a diffusion-controlled reaction in the electrochemical process (Eissa et al., 2013). In Fig. 2I showed the relationship between the peak potential (E_p) and the logarithm value of scan rate (lgv). As the scan rate increasingly, the oxidation peak potential shifted positively and the reduction peak potential shifted negatively. When $\Delta E_p > 160$ mV, the E_{pa} and E_{pc} were linearly dependent on the logarithm of v (lgv) with the regression equations of E_{pa} = 0.3014 + 0.0407 lgv (V/s) (R = 0.9909) and E_{pc} = 0.1183 – 0.0395 lgv (V/s) (R = 0.9735). Based on the Laviron theory, the apparent electron transfer rate constant was calculated as follows (Yin et al., 2010):

$$\lg\frac{k_a}{k_c} = \lg\frac{\alpha}{1-\alpha} \quad (1)$$

$$\lg k_s = \alpha\lg(1-\alpha) + (1-\alpha)\lg\alpha - \lg\frac{RT}{nFv} - \frac{2.3RT\alpha}{(1-\alpha)nF\Delta k_P} \quad (2)$$

where k_a and k_c are the slope of the straight lines for E_{pa} versus lgv and E_{pc} versus lgv, respectively, R is gas constant, T is room temperature and F is Faraday constant, n is the number of transferred electrons (n = 1). The charge transfer coefficient α, can be calculated to be 0.507 based on the Eq. (1). And the value of k_s was calculated to be 1.4 s^{-1}. As the immunosensing substrate, Au NR@PDA can improve electrochemical performance, resulting in the increased electrochemical active site and the enhanced electrochemical response.

3.2. Characterization of N/S-cGO/L-lys/Au@Pt MBs/Thi composites

Fig. 3A showed the characterization of N/S-cGO. As indicated by the TEM image, N/S-cGO possess the ultrathin layered morphology through N and S co-doping. Fig. 3B indicated that Au@Pt MBs had formed a highly uniform multi-branched structure with a regular size. In addition, morphology of Au@Pt MBs was further characterized using high-angle annular darkfield scanning transmission electron microscopy (HAAD-STEM) elemental analysis. Fig. 3C and Fig. 3D exhibited the clear color contrast of Pt (green) and Au (yellow), indicating the core-shell structure was formed successfully. As illustrated in HAAD-STEM (Fig. 3E), because of the difference in bright and dark contrast between Pt and Au, the composed of numerous Pt NPs could be easily obtained. Fig. 3F showed the SEM image of N/S-cGO/L-lys/Au@Pt MBs. Clearly, Au@Pt MBs were connected onto the surface of N/S-cGO by using L-lys as a bridge. As a useful method, Raman spectroscopy was further used to characterize N/S-cGO and N/S-cGO/L-lys/Au@Pt MBs. As shown in Fig. 3G, the two typical characteristic peaks (a D-band at 1350 cm^{-1} and a G-band at 1610 cm^{-1}) of the N/S-cGO (curve a) and N/S-cGO/L-lys/Au@Pt MBs (curve b) were obtained (Chen et al., 2016). The calculated intensity ratio of N/S-cGO/L-lys/Au@Pt MBs (I_D/I_G = 1.077) was higher than that of N/S-cGO (I_D/I_G = 0.942) owing to the increased structural defects and distortion after the binding of L-lys and Au@Pt MBs. Meanwhile, EDS was used to analyze the ingredient of the composites, also illustrating the N/S-cGO/L-lys/Au@Pt MBs were composed of C, N, O, S, Au and Pt elements (Fig. S2). In brief, these observations suggested that N/S-cGO/L-lys/Au@Pt MBs was synthesized successfully.

Fig. 3H showed the UV–vis absorption spectra of Thi and N/S-cGO/L-lys/Au@Pt MBs/Thi composites. Two characteristic adsorption peaks (a UV region at 270 nm and a visible region at 600 nm) of the Thi (curve a) and N/S-cGO/L-lys/Au@Pt MBs/Thi (curve b) were observed, which indicated that the attachment of the Thi molecules in the N/S-cGO/L-lys/Au@Pt MBs. In order to further confirm the successful immobilization of the Thi molecules, CV was used and tested by recording the current response in PBS solution. As seen in Fig. 3I, the bare GCE showed no obvious redox peaks in the potential range studied (curve a). When N/S-cGO/L-lys/Au@Pt MBs modified GCE, the double layer capacitance current was higher than the bare GCE and insignificant redox peaks were observed (curve b). While the N/S-cGO/L-lys/Au@Pt MBs/Thi composites modified GCE, a pair of reversible redox peaks with cathodic and anodic peak potentials were observed (curve c), indicating

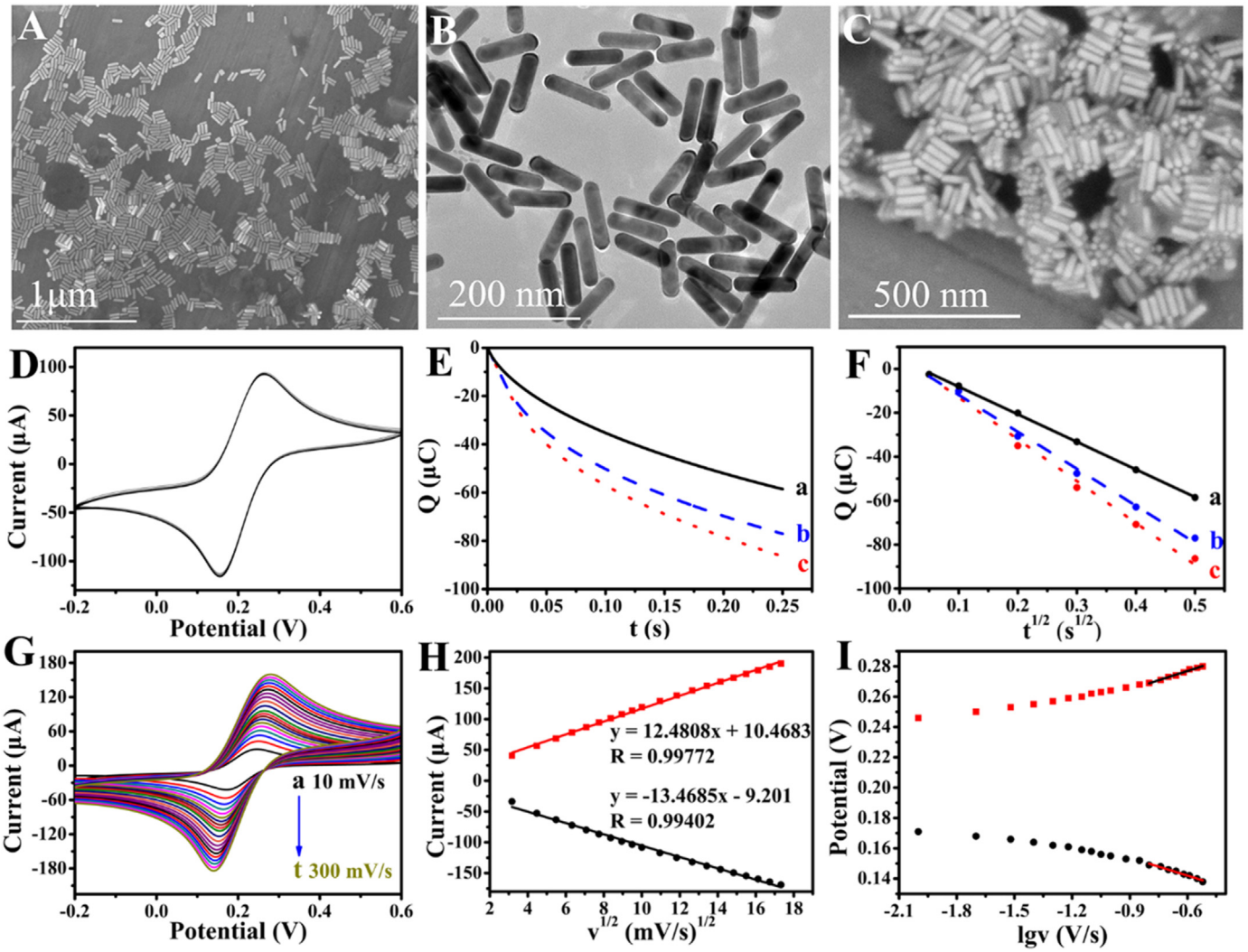

Fig. 2. (A) SEM image and (B) TEM image of Au NR. (C) SEM image of Au NR@PDA. (D) CV of Au NR@PDA modified bare GCE (sweep speed: 50 mV/s) continuous sweep 60 times. (E) Plot of Q-t curves and (F) plot of Q-$t^{1/2}$ curves for bare GCE (a), Au NR/GCE (b) and Au NR@PDA/GCE (c). (G) CV curves of the Au NR@PDA modified electrodes at different scan rates (from a to t, 10, 20, 30, 40, 50, 60, 70, 80, 90, 100, 120, 140, 160, 180, 200, 220, 240, 260, 280 and 300 mV/s). (H) The linear relationship between the anodic and cathodic peak currents versus scan rate. (I) The fitting straight curves of lgv versus potential.

Thi molecules were modified on N/S-cGO/L-lys/Au@Pt MBs successfully.

Fig. 3J showed the CV measurement of N/S-cGO/L-lys/Au@Pt MBs/Thi composites modified GCE at different scan rates (10–300 mV/s) in PBS solution. It is clearly found that the peak currents enhanced linearly with increasing scan rates. Meanwhile, the linear relationships with good correlation coefficients were observed in Fig. 3K, all the above results indicating the redox process of N/S-cGO/L-lys/Au@Pt MBs/Thi composites is a fast and surface-confined process on the surface of electrode (Zhai et al., 2016).

As illustrated in Fig. 4A, N/S-cGO, N/S-cGO/L-lys/Au@Pt MBs and N/S-cGO/L-lys/Au@Pt MBs/Thi composites were modified GCE respectively and tested by *i-t* to illustrate the electrocatalytic activity for H_2O_2 reduction, the results showed that the current signal increased successively. Compared with N/S-cGO (curve a) and N/S-cGO/L-lys/Au@Pt MBs (curve b), the N/S-cGO/L-lys/Au@Pt MBs/Thi composites (curve c) exhibited a larger current change after H_2O_2 was added into the PBS solution. The results indicated that N/S-cGO/L-lys/Au@Pt MBs/Thi composites had a good electrocatalytic effect for H_2O_2 reduction, this phenomenon was attributed to the specific electrocatalytic activity of Au@Pt MBs and electron mediator effect from Thi molecules. Therefore, the N/S-cGO/L-lys/Au@Pt MBs/Thi composites were used as the Ab_2 label to increase the current response and further improve the sensitivity of the designed cTnI immunosensor.

3.3. Electrochemical behavior of the stepwise fabrication of the immunosensor

To confirm the stepwise procedure of the sandwich-type immunosensor fabrication, we applied EIS and CV methods to characterize different assembled electrodes. As demonstrated in Fig. 4B, C, Au NR@PDA modified electrode (curve b) had an obvious increased CV current and decreased the charge transfer resistance (Ret) of EIS compared with the bare GCE (curve a), indicating the Au NR@PDA with large surface area and excellent conductivity promoted the electron transfer. However, when Ab_1 (curve c), BSA (curve d), cTnI (curve e) and N/S-cGO/L-lys/Au@Pt MBs/Thi-Ab_2 (curve f) were stepwise assembled onto the Au NR@PDA, a successively decreased trend of the redox peaks in CV and an increasing Ret response in EIS were acquired. Due to the biological molecular occupies and blocks part of the electronic transmission channel, and increases the resistance when ferricyanide passes through the film, thus reducing the redox peaks current and increasing the Ret response. These results confirmed the successful fabrication of the sensing interface.

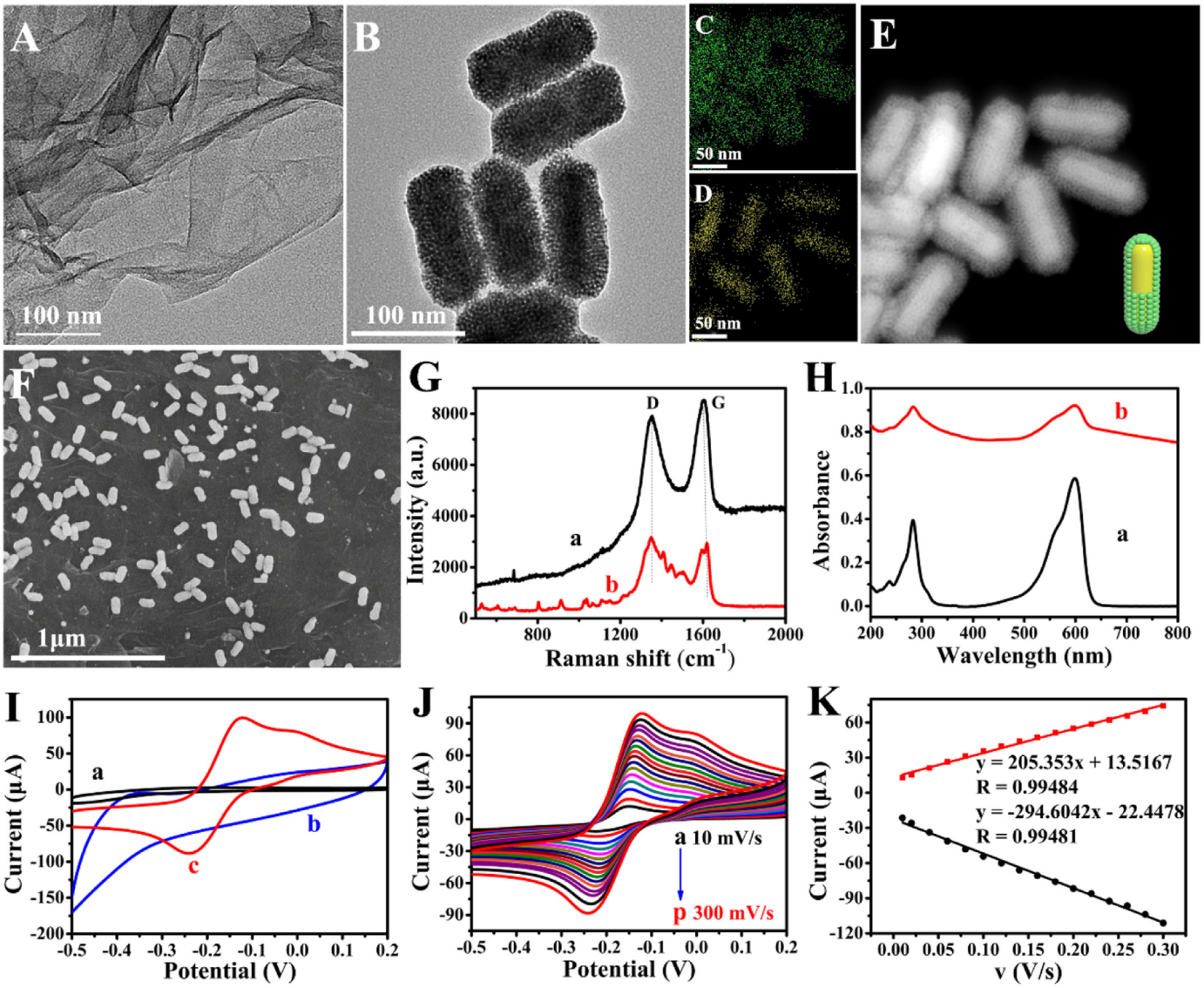

Fig. 3. (A) TEM image of N/S-cGO. (B) TEM image of Au@Pt MBs. (C) Pt elemental mapping. (D) Au elemental mapping. (E) HAAD-STEM of Au@Pt MBs. (F) SEM image of N/S-cGO/L-lys/Au@Pt MBs. (G) Raman spectra of N/S-cGO (a) and N/S-cGO/L-lys/Au@Pt MBs (b). (H) UV–vis spectrum of Thi (a) and N/S-cGO/L-lys/Au@Pt MBs/Thi (b). (I) CV of bare GCE (a), N/S-cGO/L-lys/Au@Pt MBs/GCE (b) and N/S-cGO/L-lys/Au@Pt MBs/Thi/GCE (c) modified GCE in 0.1 M PBS buffer (pH = 7.0). (J) CV curves of the N/S-cGO/L-lys/Au@Pt MBs/Thi modified electrodes at different scan rates (from a to p, 10, 20, 40, 60, 80, 100, 120, 140, 160, 180, 200, 220, 240, 260, 280 and 300 mV/s). (K) The linear relationship between the anodic and cathodic peak currents versus scan rate.

3.4. Optimization of the experimental conditions

To achieve sensitive cTnI detection, it is crucial to optimize several variables of the immunosensor system, including pH of PBS, the concentrations of Au NR@PDA and N/S-cGO/L-lys/Au@Pt MBs/Thi.

The pH of the buffer solution is an important parameter for analyzing the performance of immunosensors. On the one hand, the value of pH can effect on the affinity between the protein and the transducing material of the electrode surface. On the other hand, the highly acidic or alkaline pH may cause protein denaturization. Fig. 4D showed influence of pH value on the signal response at various immunosensors in a series of pH of PBS, with the variation of pH from 6.0 to 7.0, the current signals increased and then decreased with the pH from 7.0 to 7.8. Accordingly, the optimum pH (7.0) was applied in the following analytical experiments.

The amount of capture antibody immobilized on GCE surface was an important factor affecting the immunosensor electrochemical response, which depended on the concentration of Au NR@PDA. As shown in Fig. 4E, with the concentration of Au NR@PDA increased from 3.0 to 7.0 μL, the numbers of the antibody and the current responses were both increased rapidly. When the concentration becomes higher than 7.0 μL, the increasing film thickness of Au NR@PDA may lead to an increase of interface electron transfer resistance. Therefore, 7.0 μL was proved to be the optimum concentration of substrate material for prepared immunosensor. Besides, the concentration of N/S-cGO/L-lys/Au@Pt MBs/Thi is also investigated. As presented in Fig. 4F, the electrochemical signal increased and reached its maximum at 3.0 mg/mL. Due to the appropriate concentration of N/S-cGO/L-lys/Au@Pt MBs/Thi-Ab_2 not only ensures the successfully specific binding between antigen and antibody but also efficiently enhances the catalytic performance; however, in high concentration, the excessively thick film of N/S-cGO/L-lys/Au@Pt MBs/Thi-Ab_2 could hinder the electron transfer because of the increased interface resistance. Therefore, the optimal concentration of N/S-cGO/L-lys/Au@Pt MBs/Thi was selected as 3.0 mg/mL.

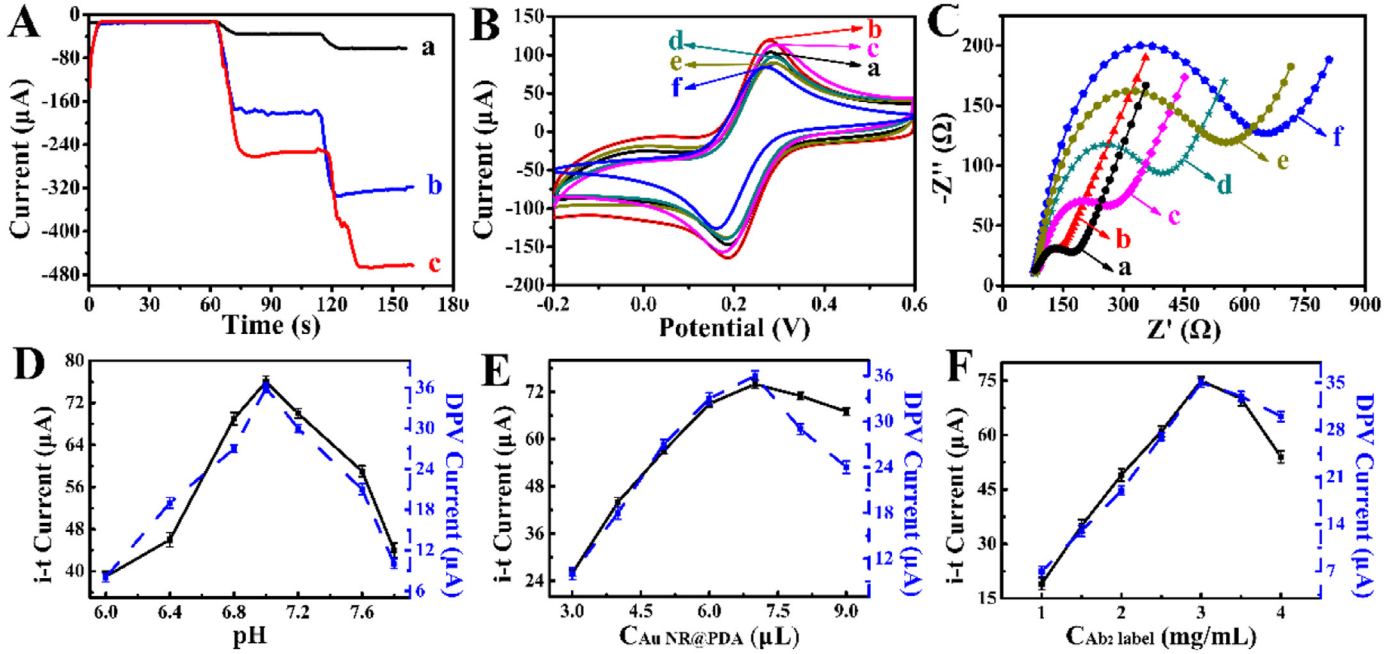

Fig. 4. (A) The studies of *i-t*: N/S-cGO (a), N/S-cGO/L-lys/Au@Pt MBs (b) and N/S-cGO/L-lys/Au@Pt MBs/Thi (c). (B) CV and (C) EIS method for each fabricated step: bare GCE (a), GCE/Au NR@PDA (b), GCE/Au NR@PDA/Ab_1 (c), GCE/Au NR@PDA/Ab_1/BSA (d), GCE/Au NR@PDA/Ab_1/cTnI (e), and GCE/Au NR@PDA/Ab_1/BSA/cTnI/N/S-cGO/L-lys/Au@Pt MBs/Thi-Ab_2 (f). The influence of experimental parameters with (D) pH, (E) concentration of Au NR@PDA and (F) Ab_2 label on the current response of the immunosensor incubated with 1.0 ng/mL cTnI (Solid Line respect the results of i-t. Dash Line respect the results of DPV). Error bar = RSD (n = 5).

3.5. Analytical performance of the proposed immunosensor

To examine the sensitivity and the quantitative analysis of the proposed immunosensor, it was studied by *i-t* (Fig. 5A) and DPV (Fig. 5C) incubating various concentrations of cTnI standard samples under the optimal experimental conditions. A good linear dependence between *i-t* current changes and the logarithm of cTnI concentration ranging from 50 fg/mL to 200 ng/mL can be obtained, and the detection limit was calculated to be 16.7 fg/mL (Fig. 5B). The fitted linear regression equation: I (μA) = 10.9196 lgC (ng/mL) + 75.2874 (R = 0.99729). Meanwhile, Fig. 5D showed that the concentrations of cTnI ranged from 750 fg/mL to 100 ng/mL had a good linear relationship between DPV current responses and the logarithm of cTnI concentration, with a detection limit of 250 fg/mL. Quantitative cTnI detection could be achieved by the linear equation: I (μA) = 5.8379 lgC (ng/mL) + 38.029 with the squared correlation coefficient of R = 0.99856. We have compared the analytical performance of the designed method with others for cTnI detection in terms of the detection range and the detection limit in Table S1. It clearly indicated that the immunosensor displayed comparable or even better analytical

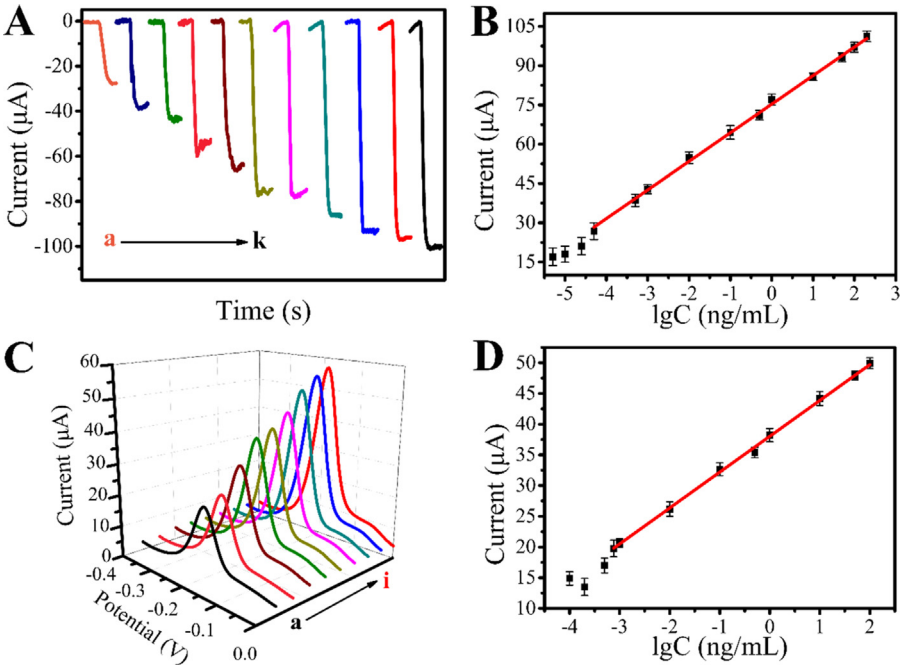

Fig. 5. Current response of the immunosensor to different concentrations of cTnI: the results of *i-t* (A) from a to k: 50 fg/mL, 500 fg/mL, 1.0 pg/mL, 10 pg/mL, 100 pg/mL, 500 pg/mL, 1.0 ng/mL, 10 ng/mL, 50 ng/mL, 100 ng/mL, 200 ng/mL, the results of DPV (C) from a to i: 750 fg/mL, 1.0 pg/mL, 10 pg/mL, 100 pg/mL, 500 pg/mL, 1.0 ng/mL, 10 ng/mL, 50 ng/mL, 100 ng/mL. Their calibration curves of the immunosensor to different concentrations of cTnI (B, D, respectively). Error bar = RSD (n = 5).

performance.

3.6. Reproducibility, specificity and stability

Some vital important characteristics of this immunosensor, including reproducibility, specificity and stability need to be tested. The repeatability experiment was performed by recording the electrochemical signals of three different concentration levels (1.0 pg/mL, 1.0 ng/mL, and 10 ng/mL) via *i-t*. As the results in Fig. S3A, the relative standard deviation (RSD) of the measurements was less than 5.0% (n = 5), suggesting the proposed immunosensor had acceptable reproducibility.

To assess the specificity of the designed cTnI immunosensor, we chose four proteins: carcinoembryonic antigen (CEA), prostate specific antigen (PSA), immunoglobulin G (IgG), alpha fetoprotein (AFP) and BSA as the interferents. In the specificity study, the concentration of cTnI is 1.0 ng/mL, while these interferents concentration is 100 ng/mL. As expected, the immunosensor current response of 1.0 ng/mL cTnI with interferents is the same as that of 1.0 ng/mL cTnI without interferents (Fig. S3B). For samples with the interferents only, the immunosensor current change has no apparent signal changes compared with the blank experiment, this was attributed to the specific recognition between antibody and antigen. The results demonstrated that cTnI detection by the designed sandwich-type immunosensor had high specificity.

Finally, the stability was also investigated by preparing and storing the immunosensor at 4 °C, and detected every three days. The response signals decrease gradually during the whole testing period, and the cTnI immunosensor also remained about 89% of its initial current signal (Fig. S3C). The experimental data revealed the good stability of the obtained immunosensor.

3.7. Real sample analysis

In order to investigate the application and reliability of the immunosensor for practical analysis, this immunosensor was used to cTnI analysis by the standard addition method (Saxberg and Kowalski, 1979). Different concentrations of cTnI (10, 100, and 1000 pg/mL) were spiked into the serum sample and the collated results were presented in Table S2. The recovery via *i-t* ranged from 98.0% to 101.9% with the RSD ranging between 2.5% and 3.9%. Meanwhile, the recovery of detecting cTnI via DPV was 99.2–101.8% and the variation of RSD ranged from 3.0% to 3.8%. The data clearly demonstrated its great potential in serum samples.

4. Conclusion

In summary, N/S-cGO/L-lys/Au@Pt MBs/Thi was explored as a double signal label in sandwich-type cTnI immunosensor. It provided an excellent catalytic ability for H_2O_2 and generated a good current response via *i-t*, meanwhile, itself can act as a signal putout to get an excellent DPV current signal. Furthermore, Au NR@PDA were employed as the substrate material, which not only accelerated the electron transfer rate of sensing interface, but enhanced the ability to immobilize Ab_1. With the help of N/S-cGO/L-lys/Au@Pt MBs/Thi and Au NR@PDA, the proposed immunosensor showed a wide linear concentration range (*i-t* results: 50 fg/mL to 250 ng/mL, DPV results: 750 fg/mL to 100 ng/mL) and a low detection limit (*i-t* results:16.7 fg/mL, DPV results:250 fg/mL). More importantly, satisfactory recoveries were acquired when the immunosensor was applied in the detection of cTnI of real-life samples. Considering the benefits of acceptable reproducibility, high sensitivity and good stability of our methods, we believe that this immunosensor will provide a potential application in clinical diagnose.

CRediT authorship contribution statement

Hui Lv: Conceptualization, Methodology, Software, Investigation, Data curation, Writing - original draft, Writing - review & editing. **Yueyun Li:** Conceptualization, Visualization, Supervision, Funding acquisition, Data curation, Resources, Project administration. **Xiaobo Zhang:** Visualization, Investigation, Data curation. **Xinjin Li:** Supervision, Validation, Resources, Project administration. **Zhen Xu:** Validation, Writing - review & editing, Resources. **Lei Chen:** Validation, Writing - review & editing. **Degang Li:** Data curation, Software, Resources, Validation. **Yunhui Dong:** Supervision, Resources, Validation.

Acknowledgments

This study was financially supported by the National Natural Science Foundation of China (Nos. 21575079), the Key Research and Development Program of Shandong Province (No. 2018GSF120001, 2018GNC110038). All of the authors express their deep thanks.

Appendix A. Supporting information

Supplementary data associated with this article can be found in the online version at doi:10.1016/j.bios.2019.03.033.

References

Anson, F., 1964. Anal. Chem. 36, 932–934.
Asif, M., Aziz, A., Ashraf, G., Wang, Z., Wang, J., Azeem, M., Chen, X., Xiao, F., Liu, H., 2018. ACS Appl. Mater. Interfaces 10, 36675–36685.
Chen, L., Song, L., Zhang, Y., Wang, P., Xiao, Z., Guo, Y., Cao, F., 2016. ACS Appl. Mater. Interfaces 8, 11255–11261.
Cho, I.-H., Lee, J., Kim, J., Kang, M.-s., Paik, J., Ku, S., Cho, H.-M., Irudayaraj, J., Kim, D.-H., 2018. Sensors 18, 207.
Eissa, S., L'Hocine, L., Siaj, M., Zourob, M., 2013. Analyst 138, 4378–4384.
Gao, Z., Li, Y., Zhang, X., Feng, J., Kong, L., Wang, P., Chen, Z., Dong, Y., Wei, Q., 2018. Biosens. Bioelectron. 102, 189–195.
He, S., Li, X., Wu, Y., Wu, S., Wu, Z., Yang, A., Tong, P., Yuan, J., Gao, J., Chen, H., 2018. J. Agric. Food Chem. 66, 11830–11838.
Hu, W., Wang, Q., Wu, S., Huang, Y., 2016. J. Mater. Chem. A 4, 16920–16927.
Lai, Y., Deng, Y., Yang, G., Li, S., Zhang, C., Liu, X., 2018. J. Biomed. Nanotechnol. 14, 1688–1694.
Lai, Y., Zhang, C., Deng, Y., Yang, G., Li, S., Tang, C., He, N., 2019. Chin. Chem. Lett. 30, 160–162.
Li, M., Wang, P., Pei, F., Yu, H., Dong, Y., Li, Y., Liu, Q., Chen, P., 2018. Sens. Actuators B: Chem. 261, 22–30.
Liu, Y., Lai, Y., Yang, G., Tang, C., Wang, Z., 2017. J. Biomed. Nanotechnol. 13, 1253–1259.
Lv, H., Li, Y., Zhang, X., Gao, Z., Feng, J., Wang, P., Dong, Y., 2018a. Anal. Chim. Acta 1007, 61–70.
Lv, H., Li, Y., Zhang, X., Gao, Z., Zhang, C., Zhang, S., Dong, Y., 2018b. Biosens. Bioelectron. 112, 1–7.
Saxberg, B.E., Kowalski, B., 1979. Anal. Chem. 51, 1031–1038.
Shen, M., Ruan, C., Chen, Y., Jiang, C., Ai, K., Lu, L., 2015. ACS Appl. Mater. Interfaces 7, 1207–1218.
Shen, Y., Shen, G., Zhang, Y., 2018. ACS Omega 3, 11227–11232.
Spain, E., Carrara, S., Adamson, K., Ma, H., O'Kennedy, R., De Cola, L., Forster, R.J., 2018. ACS Omega 3, 17116–17124.
Wen, W., Yan, X., Zhu, C., Du, D., Lin, Y., 2016. Anal. Chem. 89, 138–156.
Yáñez-Sedeño, P., González-Cortés, A., Agüí, L., Pingarrón, J.M., 2016. Electroanalysis 28, 1679–1691.
Yang, G., Lai, Y., Xiao, Z., Tang, C., Deng, Y., 2018a. Chin. Chem. Lett. 29, 1857–1860.
Ye, J., Zhu, L., Yan, M., Zhu, Q., Lu, Q., Huang, J., Cui, H., Yang, X., 2018. Anal. Chem. 91, 1524–1531.
Yin, H., Ma, Q., Zhou, Y., Ai, S., Zhu, L., 2010. Electrochim. Acta 55, 7102–7108.
Zhai, Q., Zhang, X., Li, J., Wang, E., 2016. Nanoscale 8, 15303–15308.
Zhang, A., Guo, W., Ke, H., Zhang, X., Zhang, H., Huang, C., Yang, D., Jia, N., Cui, D., 2018a. Biosens. Bioelectron. 101, 219–226.
Zhang, C., Zhang, S., Jia, Y., Li, Y., Wang, P., Liu, Q., Xu, Z., Li, X., Dong, Y., 2019. Biosens. Bioelectron. 126, 785–791.
Zhang, D., Li, W., Wang, H., Ma, Z., 2018b. Sens. Actuators B: Chem. 258, 141–147.
Zhang, J., Liu, X., Guo, X., Wu, S., Wang, S., 2010. Chem. Eur. J. 16, 8108–8116.
Zhang, L., Xia, K., Bai, Y., Tang, Y., Deng, Y., Chen, J., Qian, W., Shen, H., Zhang, Z., Ju, S., He, N., 2014a. J. Biomed. Nanotechnol. 10, 1440–1449.
Zhang, L., Xia, K., Lu, Z., Li, G., He, N., 2014b. Chem. Mater. 26, 1794–1798.
Zhang, X., Li, Y., Lv, H., Feng, J., Gao, Z., Wang, P., Dong, Y., Liu, Q., Zhao, Z., 2018a. Biosens. Bioelectron. 106, 142–148.
Zhang, X., Li, Y., Lv, H., Gao, Z., Zhang, C., Zhang, S., Wang, Y., Xu, Z., Zhao, Z., 2018b. J. Electrochem. Soc. 165, B931–B938.
Zhou, J., Duan, B., Fang, Z., Song, J., Wang, C., Messersmith, P.B., Duan, H., 2014. Adv. Mater. 26, 701–705.
Zhou, Z., Liu, R., 2017. Colloids Surf. A: Physicochem. Eng. Asp. 522, 260–265.